International Journal of Heat and Mass Transfer 182 (2022) 121918

Contents lists available at ScienceDirect

International Journal of Heat and Mass Transfer

journal homepage: www.elsevier.com/locate/hmt

Canopy-to-canopy liquid cooling for the thermal management of lithium-ion batteries, a constructal approach

Sahin Gungor[a,b,c], Erdal Cetkin[b], Sylvie Lorente[a,*]

[a] Villanova University, Department of Mechanical Engineering, Villanova, PA, 19085, USA
[b] Izmir Institute of Technology, Department of Mechanical Engineering, 35430, Turkey
[c] Izmir Katip Celebi University, Department of Mechanical Engineering, 35620, Turkey

ARTICLE INFO

Article history:
Received 17 June 2021
Revised 19 August 2021
Accepted 29 August 2021

Keywords:
Constructal design
Flow architectures
Electric vehicle
Lithium-ion battery cells
Battery thermal management

ABSTRACT

With the growing interest on electric vehicles comes the question of the thermal management of their battery pack. In this work, we propose a thermally efficient solution consisting in inserting between the cells a liquid cooling system based on constructal canopy-to-canopy architectures. In such systems, the cooling fluid is driven from a trunk channel to perpendicular branches that make the tree canopy. An opposite tree collects the liquid in such a way that the two trees match canopy-to-canopy.

The configuration of the cooling solution is predicted following the constructal methodology, leading to the choice of the hydraulic diameter ratios. We show that such configurations allow extracting most of the non-uniformly generated heat by the battery cell during the discharging phase, while using a small mass flow rate.

1. Introduction

Many countries ambition to transition from classical to green technology vehicles in order to reduce carbon emissions and the dependence to fossil fuels [1]. In this context, electric vehicles (EVs) are perceived as a great solution, presenting numerous advantages such as silent electric motors, ease of maintenance and repair, while their main disadvantages are the milage range limit, the time needed for charge and the heat generated. The electrochemical reactions occurring within the Li-ion batteries are the cause of heat production during discharge, and absorb heat during the charging phase [2,3]. These processes occur within a constrained space leading to temperature increases in the battery pack that can irreversibly damage the battery cells. The heat generated by electrochemical reactions, joule heating, and side reactions depend on many factors, such as the current capacity rate (C-rate), the battery nominal capacity, the operating temperature, the battery layer purity, the tab location, the battery shape, aspect ratio and serial-parallel configurations. Furthermore, the generated heat within the cell is heterogeneous, leading to non-uniform temperature distributions and hot spot formation on the battery surface. As a result, the battery capacity fades, and the battery layers may experience degradation and even thermal runaway [4,5]. The latter is a key issue as it may cause chain electrochemical reactions, explosion, and fire within the EV battery pack. Fig. 1 shows the main stages of progression of thermal control deficiencies and their associated risks.

Thermal control, termed as battery thermal management system (BTMS), has emerged [2,6] in the recent past to keep the battery cell and battery pack temperature in an optimal range which is ideally between 20°C and 35°C [7]. Many scientific papers were recently published with thermal management solutions based on air [6,8,9], liquid [10,11], two-phase flow [12], phase change material (PCM) [13–15], heat pipe [16–18], thermo-electric [19,20], or nano-fluid based thermal management systems [21,22]. Today, almost all the EV industry prefers liquid cooling [23,24] with high conductive plate/frame for thermal control. Among the existing solutions, cooling systems at the scale of the battery pack consist in a water jacket combined to a high thermally conductive interface material. Other configurations consist in using high thermally conductive plates inserted between the battery cells with liquid coolant circulation. At a different scale, a heat pump system can be installed within the vehicle. In such case, heat is being removed by evaporating the liquid refrigerant. This way, the system also contributes to the vehicle cabin thermal comfort.

Ethylene-glycol supplemented water mixtures are the most common liquid coolants as the batteries must also be able to accommodate cold climatic conditions. Because the thermo-physical properties of the ethylene-glycol-water mixture depend on the

* Corresponding author.
E-mail address: sylvie.lorente@villanova.edu (S. Lorente).

https://doi.org/10.1016/j.ijheatmasstransfer.2021.121918
0017-9310/

Nomenclature

a	cooling channel thickness (m)
b	cooling channel width (m)
c_p	Specific heat capacity [J kg^{-1} K^{-1}]
C	C-rate value
d	wall thickness of cooling system [m]
D_h	Hydraulic diameter [m]
DOD	depth of discharge
f	Friction factor
g	gravitational acceleration [m s^{-2}]
H	battery and cooling system height [m]
k	thermal conductivity [W m^{-1} K^{-1}]
L	length [m]
$\dot{m}$	Mass flow rate [kg s^{-1}]
n	number of branches in the canopy
Nu	Nusselt number
P	pressure [Pa]
$\dot{q}$	heat transfer rate[W]
Pr	Prandtl number
Ra	Rayleigh number
Re	Reynolds number
S	distance between the branches [m]
Sv	Svelteness number
t	time [s]
T	temperature [K]
U	average velocity [m s^{-1}]
V	velocity vector [m s^{-1}]
V_f	fluid volume [m^3]
W	battery and cooling system width [m]
$\dot{W}$	pumping power [W]

Greek letters

λ	Lagrange multiplier
μ	dynamic viscosity [Pa.s]
ν	kinematic viscosity [m^2 s^{-1}]
ρ	density [kg m^{-3}]
Φ	aggregate function

Subscripts

b	battery cell
br	branch
in	inlet region
init	initial value
out	outlet region
path	flow path
ref	reference

mass fraction of the various components, they can be varied depending on the application strategy and technical conditions [25].

We propose in this work an approach to battery thermal management through the lenses of constructal design. The methodology is derived from the constructal law which expresses the natural tendency of flow systems of morphing in time to facilitate the access to the currents flowing through them [26,27]. The change in configuration happens in the pursuit of decreasing the thermodynamics imperfections inherent to any kind of flow systems [28–30]. Examples can be found in biological systems as in the dendritic vasculature of blood flow in a liver [31], or in engineering problems. In the latter, advances have been proposed in the design of earth-air heat exchangers by configuring the underground network to use the working fluid with higher efficiency [32–34] while accounting for both latent and sensible heat exchanges [35,36]. Energy storage is also a domain in which the morphing of the flow architecture allows to improve the heat exchanges. This is typically the case for latent thermal energy storage where the heat transfer mechanisms – convection and conduction – dictate the system configuration [37,38]. Thermochemical energy storage offers design opportunities by allocating the reacting salt volume in such a way that the chemical reaction advancement is enhanced, together with the heat released/stored while the overall pressure losses are decreased [39,40]. The common lesson learned from these examples from the thermo-fluid domain is that bold changes in the flow configuration are key for efficiency improvements. Canopy-to-canopy architectures are a vivid illustration of such changes. Departing from classical configurations based on fluid flowing through serpentine pathways, a canopy-to-canopy design consists in a single stream flowing through two tree trunks in parallel connected through their canopy [41]. The choice in diameter ratios of the connecting tubes allows decreasing the overall pressure losses, while the changes in the aspect ratio of the ensemble lead to improve the thermal exchanges [42–44].

This paper aims at testing canopy-to-canopy based systems for cooling the cells of battery packs used in electrical vehicles. The design of such constructal architectures is first explained. Then a numerical model expressing the heat generated during a battery cell discharge is developed and validated as it is during the discharging phase that the battery cell experiences the highest thermal stresses. The model is completed with the description of the cooling fluid transient behavior. The canopy-to-canopy configurations modeling shed lights on the thermal efficiency of the systems.

2. Canopy-to-canopy Design

A typical battery pack is presented in Fig. 2. The thermal management strategy pursued here consists in inserting very thin cooling elements between the cells. Each cooling element is a high thermal conductivity metallic envelop (typically made of aluminum) through which the coolant flows at a controlled mass flow rate following designed channels. The cooling elements are connected to a plenum providing the inlet fluid, and another plenum on the opposite side of the battery pack collects the now heated fluid. The alternation of cells and cooling elements allows selecting a control volume made of one cell and one cooling element, assuming that the battery pack contains enough cells to neglect the edge effects.

The simplest cooling element to investigate is shown in Figs. 3 a and c. The fluid enters from the top left side, near the two tabs, and exits oppositely, through the bottom right outlet. Next, we rely on previous work [42–45] to design canopy-to-canopy configurations, an example of which is provided in Figs. 3b and d. Departing from the reference case of Fig. 3a, a canopy-to-canopy design is made of one inlet channel to which parallel and perpendicular channels are connected, as the trunk of a tree with the branches of its canopy. Symmetrically, the parallel branches are connected to an outlet channel, which itself is parallel to the initial inlet duct. The inlet and outlet channels have the same length and cross section. The parallel branches of the canopy have identical length and cross section. The thickness of the cooling element, regardless its configuration, remains constant as the spacing between the cells is not a degree of freedom.

When moving from the reference case to canopy-to-canopy designs, the fluid volume is decreased by 28%. Then, from one canopy-to-canopy configuration to another one, the fluid volume remains fixed.

The fluid volume is given by Eq. (1) in the reference case and Eq. (2) for the canopy-to-canopy configurations.

$$V_{f,ref} = a[2\ b_{in}S + HW] \tag{1}$$

$$V_f = a[2b_{in}(W+S) + nb_{br}H_{br}] \tag{2}$$

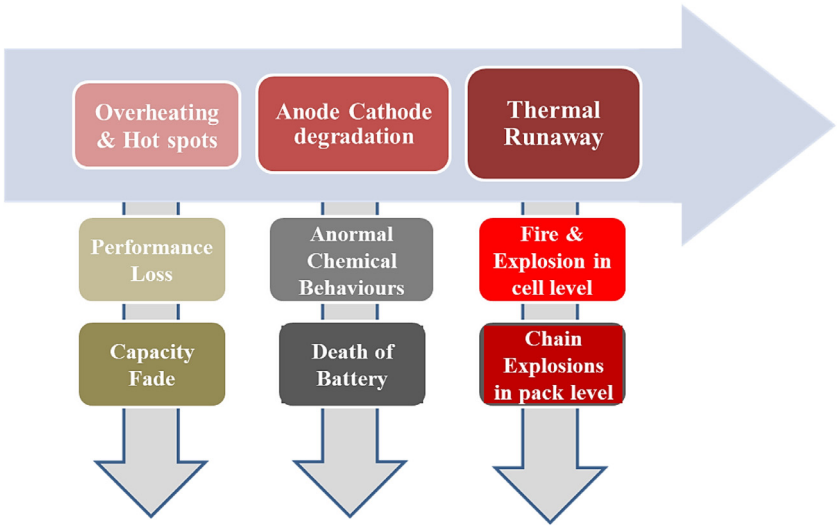

Fig. 1. Main risks associated with the lack of thermal control of Li-ion batteries.

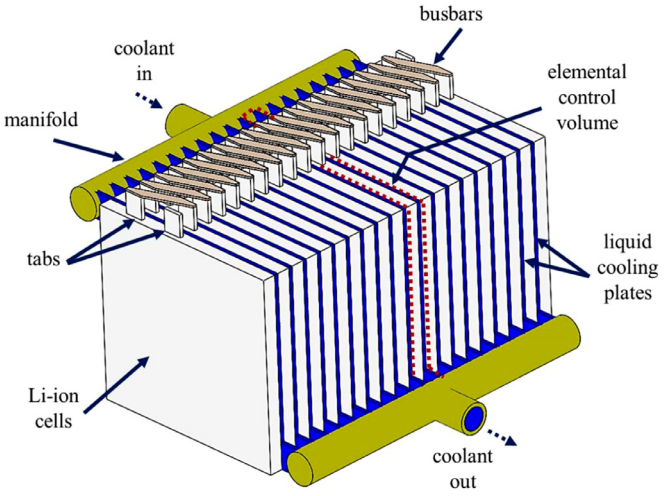

Fig. 2. Battery pack with liquid-cooled BTMS.

where, a is the cooling channel thickness, b_{in} is the inlet width (identical to the outlet width), b_{br} is the branch width, S is the distance in between the branches, W is the cooling system width, and n is the number of branches. The Li-ion battery cell dimensions ($W = 0.107\ m$ and $H = 0.102\ m$) are constant and correspond to the battery cell tested to validate own approach. We have:

$$W = 2d + nb_{br} + (n-1)S \tag{3}$$

$$H = 2b_{in} + H_{br} \tag{4}$$

where, d is the aluminum frame wall thickness and H is the total height of the cooling system (see Fig. 3).

The configuration of a canopy-to-canopy architecture starts with the search for the hydraulic diameter ratio leading to minimum pressure losses. This is based on the assumption that local losses are negligible [41,42], and can be assessed through a non-dimensional parameter, the Svelteness number [46], defined as the ratio of the external and internal length scales of the flow system. We have [43,46]:

$$Sv = L_{path}\frac{H/W}{V_f^{1/3}} \tag{5}$$

where L_{path} is the flow path length which is equivalent to the total length of the canopy-to-canopy flow channels. As shown in [46], $Sv > 10$ ensures that the pressure losses are essentially linear and local losses can be discarded.

The hydraulic diameter of the trunk channels of cross section $a \times b_{in}$ is $2a$, as $a \ll b_{in}$. Without knowing a priori if the same assumption can be made on the branches of the canopy, the branch hydraulic diameter was kept as $2ab_{br}/(a+b_{br})$. The general expression of the pressure losses is given by [47],

$$\Delta P = f\frac{4L}{D_h}\left(\frac{1}{2}\rho U^2\right) \tag{6}$$

where L is the channel length, D_h is the hydraulic diameter and U is the average velocity. The friction factor f is $24/Re_{Dh}$ in the case of a trunk, and $\frac{a^2+b_{br}^2}{(a+b_{br})^2}\frac{24}{Re_{Dh}}$ for the branches. Considering that the distribution of the inlet mass flow rate $\dot{m}$ from trunk to branches separated by a distance S is uniform and equal to $\dot{m}/n$, we have from inlet to outlet:

$$\Delta P = \frac{12\nu\dot{m}}{a^3}\left[\frac{S\left(2+\sum_{i=1}^{n-1} i/n\right)}{b_{in}} + \frac{H\left(a^2+b_{br}^2\right)}{b_{br}^3}\right] \tag{7}$$

The hydraulic diameter ratio leading to minimum pressure losses while maintaining V_f the total fluid volume and a constant (Eq. 2) was obtained by means of the method of the Lagrange multipliers. An aggregate function $\Phi = \Delta P + \lambda V_f$ was first constructal, where λ is the Lagrange multiplier. Then the values of λ for which the derivatives $\partial\Phi/\partial b_{in}$ and $\partial\Phi/\partial b_{br}$ are null were determined, leading to a relationship between b_{in} and b_{br} expressed by:

$$b_{in} = \left[\frac{n}{2}\frac{S}{(W+S)}\left(2+\sum_{i=1}^{n-1} i/n\right)\frac{b_{br}^4}{\left(3a^2+b_{br}^2\right)}\right]^{1/2} \tag{8}$$

The numerical values of b_{in} and b_{br} were obtained for a given fluid volume and a given dimension by means of a code written in Wolfram Mathematica. They are given in Table 1 for n = 3,5,6,7,10 and 20 branches.

3. Model and Validation

The temperature field in the cooling system and at the battery cell surface, and the coolant velocity field were determined by solving the conservation equations of mass, momentum, and energy in transient regime with the appropriate initial and boundary conditions. In the incompressible cooling fluid, we have:

$$\nabla V = 0 \tag{9}$$

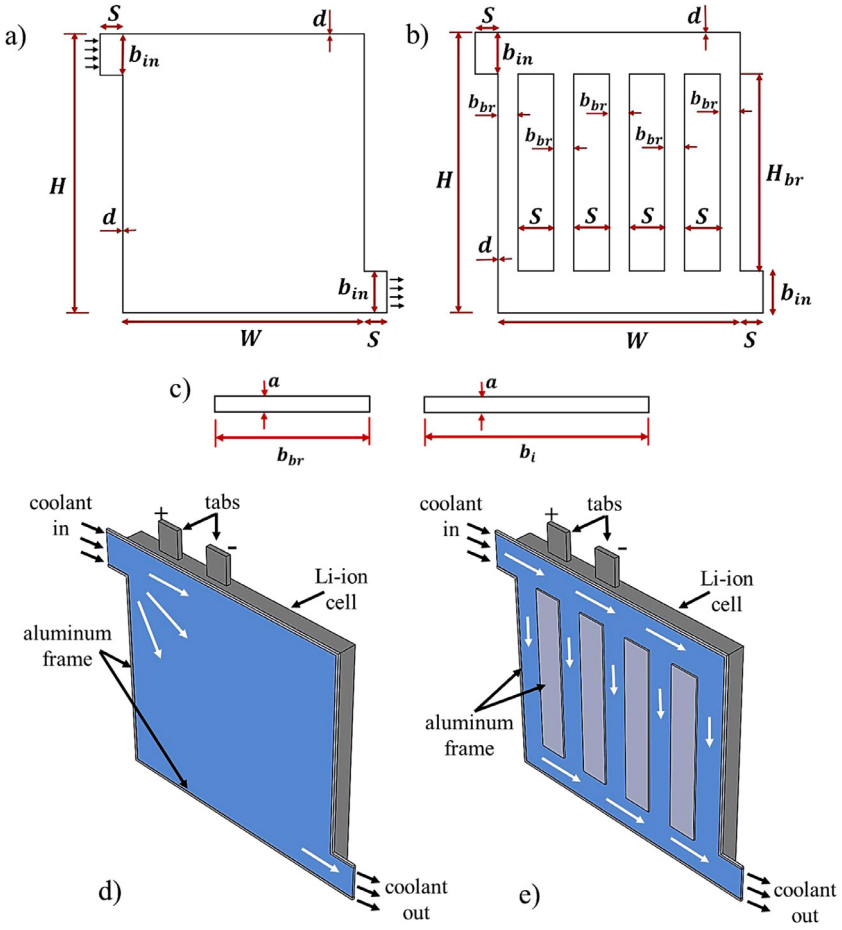

Fig. 3. Cooling systems for (a) and (d) reference case, (b) and (e) canopy-to-canopy design, and (c) its cross section.

Table 1
Characteristics of the canopy-to-canopy designs.

Flow Architectures	V_f (m^3)	a (m)	b_i (m)	b_{br} (m)	*Sv*
3-branches	$7.64 \times \times 10^{-6}$	0.001	0.0169	0.0156	22.21
5-branches	7.64×10^{-6}	0.001	0.0164	0.0120	28.04
6-branches	7.64×10^{-6}	0.001	0.0154	0.0105	31.84
7-branches	7.64×10^{-6}	0.001	0.0144	0.0093	35.93
10-branches	7.64×10^{-6}	0.001	0.0120	0.0069	48.78
20-branches	7.64×10^{-6}	0.001	0.0077	0.0036	94.41

Table 2
Material properties used in the simulations [51].

Materials	ρ(kg/m^3)	c_p (J/kgK)	k (W/mK)	μ (Pa.s)
Coolant	1073	3474	0.41	0.002605
Aluminum Frame (1)	2719	871	202	–
Battery cell (2)	2092	678	18.2	–
Positive tab (3)	2719	871	202	–
Negative tab (4)	8978	381	387.6	–

$$\rho_f \frac{DV}{Dt} = -\nabla P + \mu_f \nabla^2 V + g \tag{10}$$

$$\rho_f \, c_{p,f} \frac{DT}{Dt} = k_f \nabla^2 T \tag{11}$$

where V is the velocity vector, D/Dt stands for the material derivative, and the subscript f is for fluid. ρ is the density, P is the pressure, μ is the dynamic viscosity, g is the gravitational acceleration, c_p is the heat capacity at constant pressure, T is the temperature, and k is the thermal conductivity. Note that the flow remains laminar.

The energy equation is also written in the metallic frame with the corresponding material properties. In the case of the battery cell, the energy equation requires an additional term due to the exothermic/endothermic processes occurring during the cell discharge/charge. The heat equation is also solved in the positive and negative tabs, keeping in mind that there is no heat generated in the tabs.

$$\rho_i c_i \frac{\partial T}{\partial t} = k_i \nabla^2 T + q_i''' \tag{12}$$

where the subscript $i = 1$ for the metallic frame, 2 for the battery cell, 3 for the positive tab, and 4 for the negative tab (see Table 2). The volumetric generated heat q_i''' is null except for $i = 2$ (battery cell).

The generated heat is obtained by modeling the battery cell behavior through a Multi-Scale Multi-Domain approach [48,49], accounting for the thermal and electrical fields. In this approach, the heat generated by the electrochemical reactions within the cell is obtained by solving the conservation of electric charge for the positive and negative electrodes in combination with an equivalent electric circuit made of three resistances and two capacitances as in Chen and Rincon-Mora's work [50]. The main factors contributing to the generated heat are Joule heating and the heat generated while the cell open circuit voltage fluctuates with temperature for each value of the battery cell state of charge. The latter generated heat is usually termed as reversible heating [3]. The battery cell has the geometrical and electrochemical characteristics of a Kokam battery cell (nominal voltage 3.7 V, capacity 7.5 Ah, discharge at 5 C rate).

When modeling a cell within a battery pack, we assumed that all the walls of the battery cell are adiabatic except for the one in

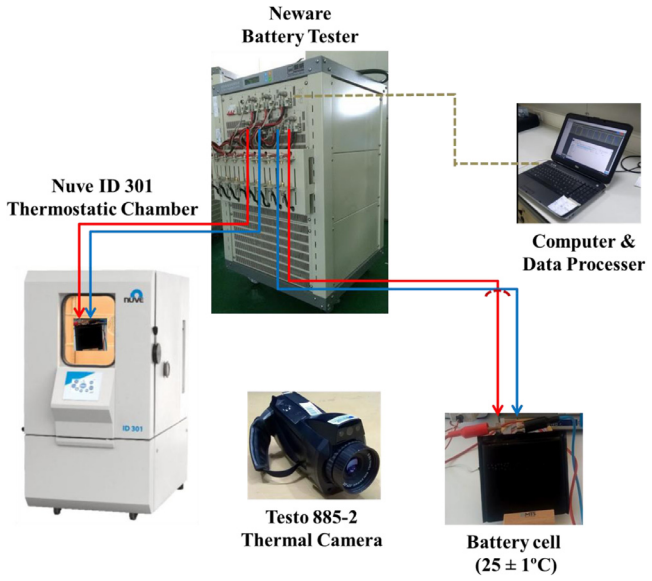

Fig. 4. Experimental set-up of the Li-ion battery cell tested in a chamber at controlled temperature.

contact with the cooling system. In such case, we account for heat flux continuity. The fluid enters the cooling system at fixed temperature T_{in} and mass flow rate $\dot{m}$. It exits at atmospheric pressure. A no-slip boundary condition is applied everywhere in the cooling device. The metallic envelop that contains the liquid is adiabatic in its top, bottom and lateral faces, together with the vertical face opposite to the battery cell (see Fig. 3). As mentioned already, heat continuity is written with the cell assuming perfect thermal contact. The material properties are provided in Table 2. The fluid is a mixture of water and ethylene-glycol, classically used in batteries for cooling [51]. The simulations were conducted with $T_{in} = 20°C$ and $\dot{m}$= 0.3 to 1 g/s, ensuring to a Reynolds number ranging between 15 and 60, depending on the inlet cross section. We considered that the flow regime was fully developed, as the entrance length is less than 1 mm. Initially, the entire system was at a temperature $T_{init} = 20°C$, while the fluid was motionless.

A mesh sensivity analysis was conducted, leading to 1.2×10^6 nodes. The mesh size was varied between 1.4×10^5 and 2.6×10^6 for the entire three-dimensional domain. The criteria chosen were on the maximum battery cell temperature and coolant outlet temperature values. The numerical model was based on the SIMPLE algorithm. The time step was determined after several trials in the search for a compromise with the needed computational time. The time step used in all the investigated models was 1 s, with at least 20 iterations for each time step. The convergence criteria were 10^{-6} for the conservation equations.

The validation of the modeling approach was made by comparing the temperature distribution on the face of the battery to experimental data. A detailed presentation of the experimental set-up is provided in Fig 4. The Li-ion battery cell which geometry and characteristics are identical to the model (Kokam SLPB75106100), had a nominal voltage of 3.7 V and a capacity of 7.5 Ah. The battery cell was placed in a thermostatic chamber at 25°C. The chamber was ventilated and the air velocity was measured, allowing calculating the corresponding forced convection coefficient. The discharging rate was 5C (fast discharging conditions).

When the battery cell was fully discharged (2.8 V, cut-off voltage), the temperature map on the battery cell surface was captured with a thermal camera (Testo 885–2) and monitored. The battery cell was placed in a thermostatic chamber at 25°C. The chamber was ventilated and the air velocity was measured, allowing calculating the corresponding forced convection coefficient. The discharging rate was 5 C (fast discharging conditions).

The boundary conditions in the model were adapted to the experimental case: the faces of the battery cell were submitted to a constant ambient temperature of 25°C with a forced convection heat transfer coefficient of 35.6 W/m^2K. This value was determined from $Nu = 0.664\, Re_H^{1/2} Pr^{1/2}$, a correlation in forced convection with $Re_H = 1.3 \times 10^4$ [47]. The Reynolds number was obtained by measuring the average velocity with a digital anemometer located above the battery cell. Fig. 5 shows the experimental and numerical temperature maps at full discharge. Note the non-uniform temperature distribution over the cell surface, with temperatures ranging from 47.5°C to 51.3°C. As the accuracy of the temperature map obtained with the infrared camera is of ±2% reading, we considered that the numerical approach was validated. Fig. 5 gives also the numerical and experimental voltage change during the 12 min of the discharge process. The agreement is also very good.

4. Results and Discussion

4.1. Reference case

We start with a reference case consisting in filling with heat transfer fluid the entire space delimited by the two aluminum plates of dimensions H×W. Then we move to canopy-to-canopy configurations from 3 to 20 branches in the search for a fluid volume reduction while maintaining the thermal integrity of the cell. The fluid volume is constant whatever the number of branches and represents 72% of the reference case. For the sake of conciseness, only the 5-branches case will be detailed, the other cases are given in the Appendix. The fluid enters at a fixed temperature of $T_{in} = 20°C$. The mass flow rate was decreased to the minimum value allowing the cell temperature to remain below the critical temperature of 35°C. The mass flow rate that corresponds to this threshold is $\dot{m} = 0.3$ g/s. The results are presented for this value. Figure 6a depicts the temperature distribution on the battery cell surface in the reference case at 5%, 25%, 50%, 75% of the total depth of discharge (DOD), while Fig. 6b shows the temperature map at the end of the discharge, and Fig. 6c gives the temperature map in the case of the canopy-to-canopy design made of 5 branches.

As seen in Fig. 5 which is a case without any cooling aid, heat is being generated in the vicinity of the tabs. Fig. 6 shows that the coolant circulation contributes to avoiding the peak of temperature while moving the zone of high temperature towards the bottom right of the battery cell surface. A similar result is obtained with the canopy-to-canopy architecture, even though the volume of the heat transfer fluid is drastically decreased. Furthermore, the hot spot zone is also significantly reduced, moving from 66.6% of the plate temperature above 31.2°C for the reference case (Fig. 6b) to 40.8% with the canopy-to-canopy cooling system with 5 parallel branches (Fig. 6c).

4.2. The need for the metallic plate

A lighter version of the cooling system could consist in adjusting the metallic frame to correspond exactly to the heat transfer fluid pathway. The results show that initially the temperature increase is similar in both cases. Yet, the presence of the highly conductive plate allows maintaining a lower maximum temperature. This maximum temperature remains quasi constant during most of the time of discharge. The results, obtained with the same boundary conditions as previously, are shown in Fig. 7. We gathered in this figure the temperature distribution on the battery cell surface with or without the metallic plate covering the cell surface, at the end of the discharge. 14.4% of the battery cell sur-

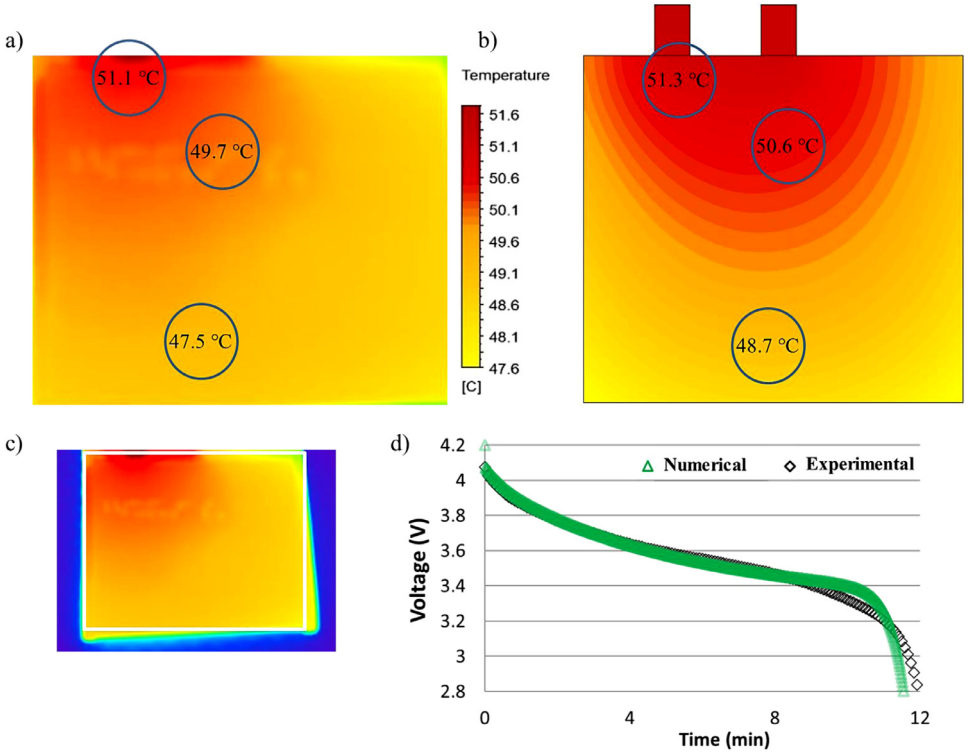

Fig. 5. Temperature distribution on the surface of the battery cell at the end of discharge (at a rate of 5C), (a) experimental and (b) numerical results. (c) Example of image for the IR camera. (d) Experimental and numerical voltage as a function of time.

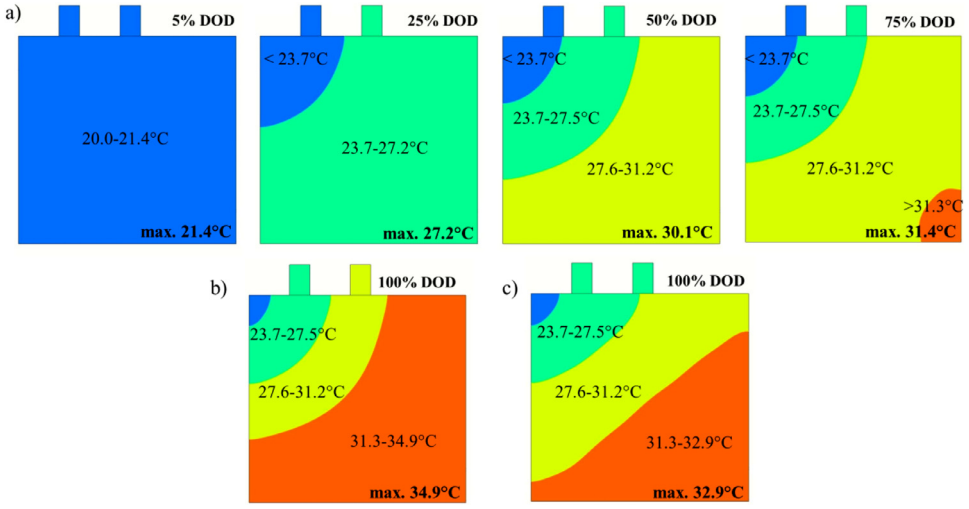

Fig. 6. Temperature maps on the surface of the battery cell as a function of the depth of discharge (DOD) for (a) the reference case when the DOD goes from 5% to 75%, (b) the reference case when the DOD is 100%, and (c) for a 5-branches canopy-to-canopy design.

face remains above 35°C when the cooling system is without the aluminum plate. As shown in Fig 7b, the maximum temperature reached is 36.1°C, which is unacceptable. When the aluminum plate is present, the battery cell surface attains a maximum temperature of 32.9°C, a value below the threshold of 35°C (Fig. 7a). In sum, the aluminum plate – or cold plate – is needed, as it contributes efficiently to drive the heat emitted by the battery cell toward the fluid, facilitating the heat extraction.

4.3. Toward lighter structures

The route towards efficient and cheap solutions consists in several paths. The objective here is to maintain the battery cell below the threshold temperature value, while decreasing the amount of fluid and reducing the power of the pump that circulates the coolant. In Fig. 8 the fluid volume was decreased compared to the initial canopy-to-canopy coolant volume. The search was continued as long as the maximum temperature obtained does not go above the maximum temperature of the initial configuration (Fig. 8a and c). Note that the constructal hydraulic diameter ratio was maintained constant. The maximum volume decrease allowing respecting the maximum temperature constraint is 45% (Fig. 8b and d).

4.4. Efficiency

The heat transfer rate generated during the discharge of the battery cell $\dot{q}$ is calculated from an energy balance within a controlled volume represented by the cell.

$$m_b c_b \frac{\partial T}{\partial t} = \dot{m}_f c_{p,f} \left(T_{in} - T_{out}\right) + \dot{q} \tag{13}$$

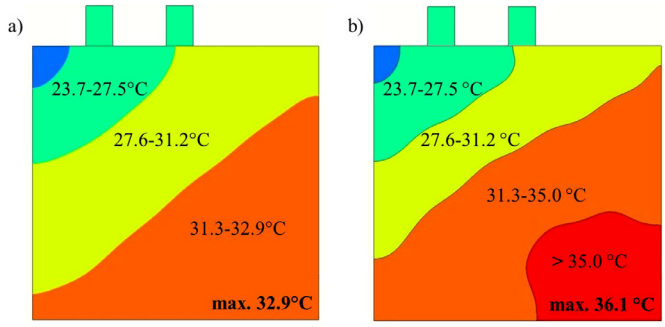

Fig. 7. Temperature distribution on the battery cell surface with a 5-branches canopy-to-canopy design (a) with aluminum frame and (b) without frame, at the end of discharge.

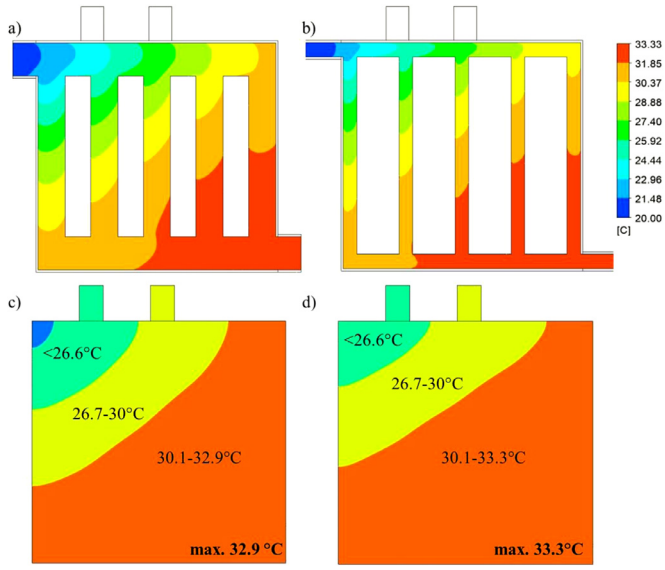

Fig. 8. Temperature distribution on the fluid side (top) and on the battery cell surface (bottom) for the initial configuration (left) and reduced volume of fluid (right).

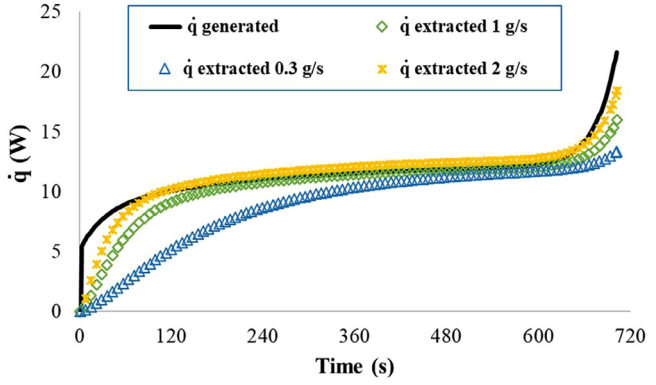

Fig. 9. Heat generation rate and enthalpy flow for 0.3 g/s and 1 g/s.

The term on the left-hand side of the Eq. 13 represents the rate of heat stored within the battery of mass m_b and heat capacityc_b. Note that T is the average temperature of the entire battery. The first term on the right-hand side is the heat exchanged with the ambient. In this work, because the battery cell surface is adiabatic except on its face in contact with the cooling system, the heat exchanged with the environment corresponds to the enthalpy flux extracted by the fluid in the cooling system.

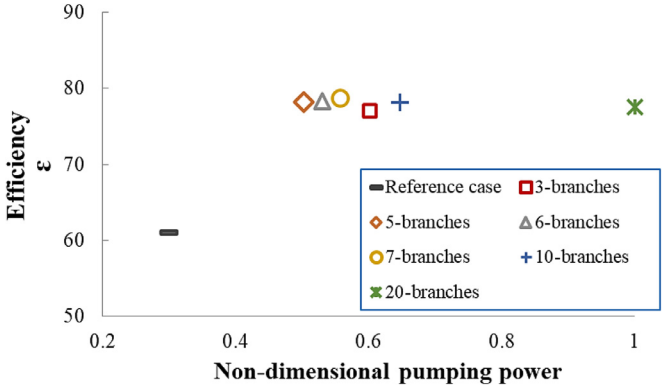

Fig. 10. Efficiency of the cooling system as a function of the pumping power.

The heat generation rate is plotted in Fig. 9 as a function of time together with the enthalpy flow changes. In addition to the case with a mass flow rate of 0.3 g/s, the configuration with $\dot{m} = 1$ g/s and 2 g/s were also considered. The canopy-to-canopy design is based on 5 branches. At the start of the discharge process, the abrupt voltage change leads to a steep increase in the heat exchanges, and none of the cooling systems is able to extract the generated heat entirely. The same situation happens at the very end of the discharge process. The cooling system with a mass flow rate of 0.3 g/s has a stronger inertia, and it is only after 500 s, or 70% of the time of discharge, that the heat extracted curve matches the heat generated one. This lasts about 14% of the time of discharge. Increasing the mass flow rate allows to match the heat generation rate during 70% of the discharge time when $\dot{m} = 1$ g/s. A higher mass flow rate, such as 2 g/s leads to a better match, and the obtained surface cell temperature reduces around 23.5 °C. Yet, this comes with increasing pumping power.

Next, the energy associated to the heat generation rate was determined, and the system efficiency ε was calculated. Efficiency is defined as the ratio of energy extracted by the cooling system, and energy produced by the battery cell. Plotted in Fig. 10 is the efficiency as a function of the pumping power required to push the coolant. In this figure, the pumping power was non-dimensionalized as $\dot{W}/\dot{W}_{max}$. We gathered the results obtained for branches going from 3 to 20 in the canopy-to-canopy designs, while keeping the fluid volume constant together with the inlet temperature value and the mass flow rate of 0.3 g/s.

The temperature distribution on the battery cell surface at the end of the discharge can be found in the Appendix for all the different numbers of parallel branches. Fig. 10 gives an overview of the ability of the cooling system to extract the heat generated by the battery cell during the discharge process and the corresponding pumping power required. The thermal efficiency of the canopy-to-canopy designs is superior to the efficiency of the reference case. During the discharge process the reference cooling system is able to extract 55% of the generated heat, while the canopy-to-canopy architectures have a thermal efficiency of 80%. This comes at the price of an increased pumping power as the non-dimensional pumping power goes from 0.3 in the reference case to 0.51 for a canopy-to-canopy configuration with 5 branches. Architecture with 3 branches has an equivalent thermal efficiency as the other canopy-to-canopy architectures but requires more pumping power to overcome the friction losses (20% as compared to 5 branches). Increasing the number of branches above 7 (while keeping the fluid volume constant) results in a strong increase in pumping with almost no improvement in the thermal efficiency.

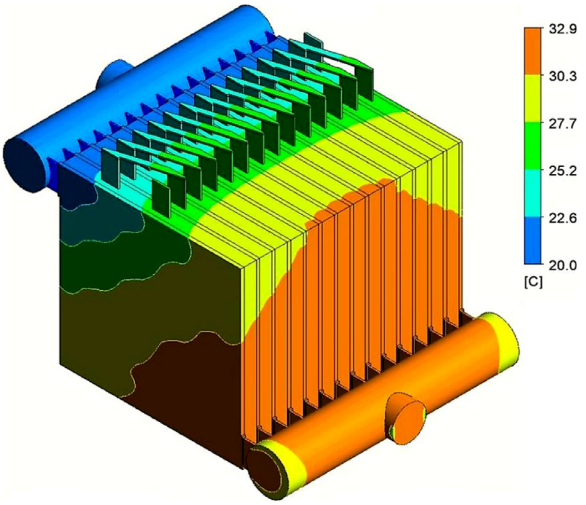

Fig. 11. Temperature distribution on the 50 V battery pack with 5 branches canopy-to-canopy architecture.

5. Conclusion

This work documented a solution for the thermal management of battery cells in electric vehicles based on a constructal canopy-to-canopy configuration approach. The main findings are as follows:

- Architectured networks made of canopy-to-canopy trees assembly use less fluid, while being as thermally efficient as a plain volume cooling system. This remains true even with a minimum mass flow rate.
- Such networks can extract most of the heat generated by a battery cell during discharge and maintain the battery cell temperature below a critical temperature value.
- A point of diminishing return exists when increasing the number of branches in parallel within the canopy, while maintaining the total volume of fluid constant. Above 7 branches in parallel, the overall pressure losses generate an increase in pumping power without leading to additional thermal improvement. The configuration with 5 branches appears to be the most interesting one with high thermal efficiency and low pumping power among the canopy-to-canopy architectures.

Finally, Fig. 11 is an illustration of the temperature distribution that can be obtained at the scale of the battery pack with 5 branches canopy-to-canopy architectures inserted between each of the 14 battery cells of the pack. The temperature distribution indicates that the maximum temperature attained is 32.9 °C, which satisfies the maximum temperature criterion.

Authors statement

SG : analytical and numerical work, EC: supervision and investigation, SL: supervision and writing

Declaration of Competing Interest

The authors declare that they have no known competing financial interests or personal relationships that could have appeared to influence the work reported in this paper.

Acknowledgement

The authors would like to acknowledge the Scientific and Technological Research Council of Turkey (TUBITAK) support program with the grant numbers of 1059B142000143 and 218M498.

APPENDIX: Thermal comparison of various canopy-to-canopy flow architectures

The canopy-to-canopy cooling systems are made of 3 to 20 branches. In each case, the ratio of hydraulic diameter follows the methodology developed in Section 2. The total fluid volume (7640 mm^3, Table 1) is identical in each case, together with the boundary and initial conditions ($T_{in} = 20\ ^\circ C$ and $\dot{m} = 0.3\ g/s$). The temperature distribution at the surface of the battery cell is reported in Fig. A1, while Fig. A2 gives the temperature distribution within the fluid domain.

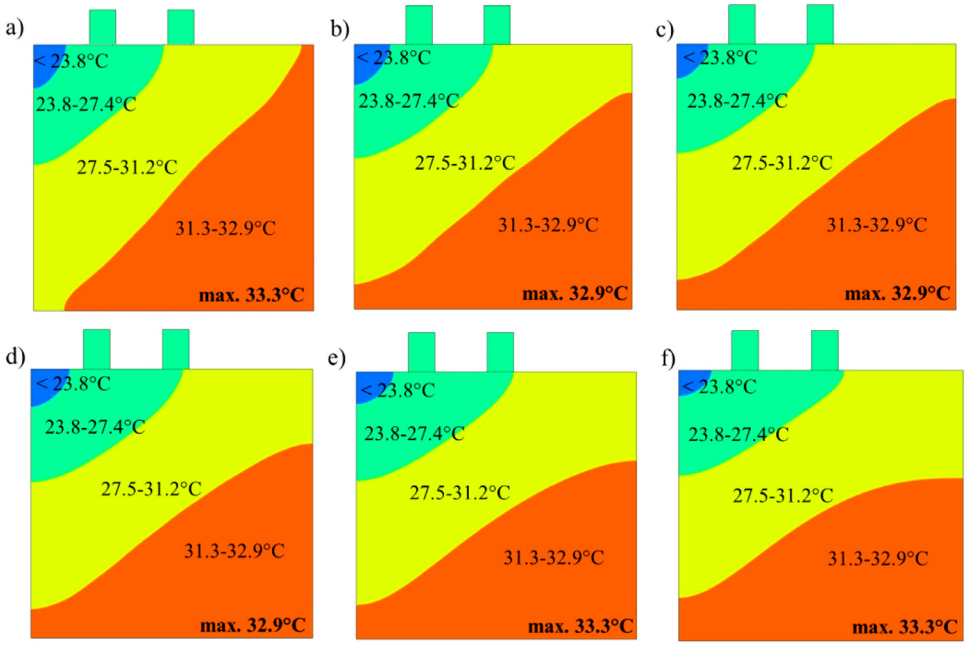

Fig. A1. Temperature maps for the battery cell surface having, (a) 3 branches, (b) 5 branches, (c) 6 branches, (d) 7 branches, (e) 10 branches, and (f) 20 branches canopy-to-canopy design.

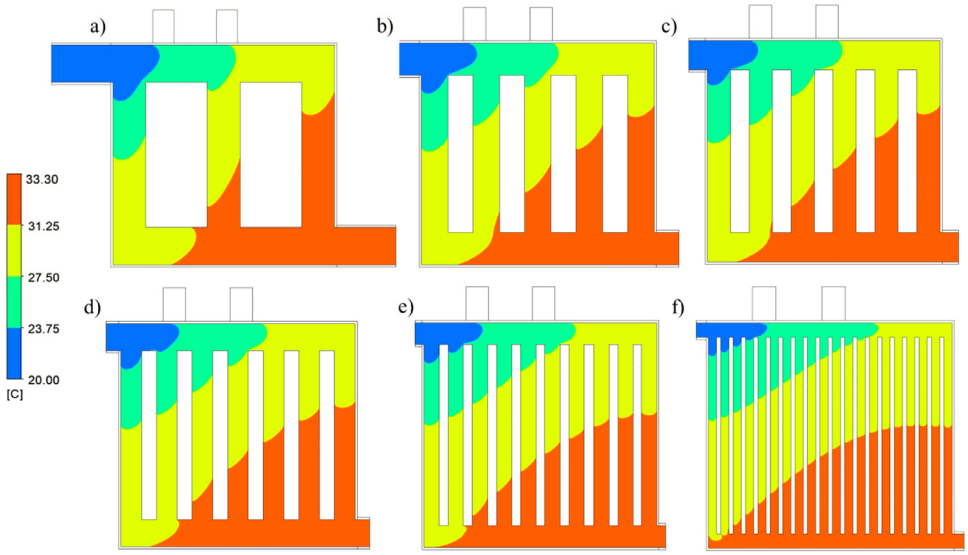

Fig. A2. Temperature distribution on the canopy-to-canopy flow architectures with (a) 3 branches, (b) 5 branches, (c) 6 branches, (d) 7 branches, (e) 10 branches, and (f) 20 branches.

The results shown in Figs. A1 and A2 correspond to the end of the discharge process. The temperature distribution at the surface of the battery cell appears to be relatively insensitive to the number of branches in parallel (Fig. A1). The main difference can be noticed at the bottom left corner of the cell, which means the furthest distance of both the inlet (top left corner) and the outlet (bottom right). In this region the surface of the cell experiencing the highest temperature values slightly increases with the number of branches. This comes in conjunction with the fluid temperature distribution as shown in Fig. A2.

References

[1] International Energy Agency (IEA)Clean Energy Ministerial and Electric Vehicles Initiative (EVI) Technology Report. Global EV Outlook 2020: Entering the decade of electric drive?, IEA Publications, 2020.

[2] Y. Xie, S. Shi, J. Tang, H. Wu, J. Yu, Experimental and analytical study on heat generation characteristic of a lithium-ion power battery, Int. J. Heat Mass Transf. 122 (2018) 884–894 (https://doi.org/10.1016/j.ijheatmasstransfer.2018.02.038).

[3] S.J. Bazinski, X. Wang, Predicting heat generation in a lithium-ion pouch cell through thermography and the lumped capacitance model, J. Power Sources 305 (2016) 97–105 (http://dx.doi.org/10.1016/j.jpowsour.2015.11.083).

[4] X. Feng, S. Zheng, D. Ren, X. He, L. Wang, H. Cui, M. Ouyang, Investigating the thermal runaway mechanisms of lithium-ion batteries based on thermal analysis database, Appl. Energy 246 (2019) 53–64, doi:10.1016/j.apenergy.2019.04.009.

[5] Z. Lei, Z. Maotao, X. Xiaoming, G. Junkui, Thermal runaway characteristics on NCM lithium-ion batteries triggered by local heating under different heat dissipation conditions, App. Therm. Eng. 159 (2019) 113847, doi:10.1016/j.applthermaleng.2019.113847.

[6] S. Gocmen, S. Gungor, E. Cetkin, Thermal management of electric vehicle battery cells with homogeneous coolant and temperature distribution, J. Appl. Phys. 127 (2020) 234902, doi:10.1063/5.0004453.

[7] A. Pesaran, S. Santhanagopalan, G.H. Kim, Addressing the impact of temperature extremes on large format Li-ion batteries for vehicle applications, 30th Int. Battery Semin. (2013) https://www.nrel.gov/docs/fy13osti/58145.pdf.

[8] X. Peng, C. Ma, A. Garg, N. Bao, X. Liao, Thermal performance investigation of an air-cooled lithium-ion battery pack considering the inconsistency of battery cells, App. Therm. Eng. 153 (2019) 596–603, doi:10.1016/j.applthermaleng.2019.03.042.

[9] K. Chen, Y. Chen, Z. Li, F. Yuan, S. Wang, Design of the cell spacing of battery pack in parallel air-cooled battery thermal management system, Int. J. Heat Mass Transf. 127 (2018) 393–401, doi:10.1016/j.ijheatmasstransfer.2018.06.131.

[10] Y. Li, Z. Zhou, W.T. Wu, Three-dimensional thermal modeling of Li-ion battery cell and 50 V Li-ion battery pack cooled by mini-channel cold plate, App. Therm. Eng. 147 (2019) 829–840, doi:10.1016/j.applthermaleng.2018.11.009.

[11] M.S. Patil, J. Seo, S. Panchal, S. Jee, M. Lee, Investigation on thermal performance of water-cooled Li-ion pouch cell and pack at high discharge rate with U-turn type microchannel cold plate, Int. J. Heat Mass Trans. 155 (2020) 119728, doi:10.1016/j.ijheatmasstransfer.2020.119728.

[12] T.M. Bandhauer, S. Garimella, S. Passive internal thermal management system for batteries using microscale liquid-vapor phase change, App. Therm. Eng. 61 (2) (2013) 756–769, doi:10.1016/j.applthermaleng.2013.08.004.

[13] J. Chen, S. Kang, E. Jiaqiang, Z. Huang, K. Wei, B. Zhang, G. Liao, Effects of different phase change material thermal management strategies on the cooling performance of the power lithium-ion batteries: A review, J. Power Sources 442 (2019) 227228, doi:10.1016/j.jpowsour.2019.227228.

[14] W. Wu, W. Wu, S. Wang, Thermal management optimization of a prismatic battery with shape-stabilized phase change material, Int. J. Heat Mass Transf. 121 (2018) 967–977, doi:10.1016/j.ijheatmasstransfer.2018.01.062.

[15] A. Lazrak, J.F. Fourmigué, J.F. Robin, An innovative practical battery thermal management system based on phase change materials: Numerical and experimental investigations, App. Therm. Eng. 128 (2018) 20–32, doi:10.1016/j.applthermaleng.2017.08.172.

[16] Z. Zhang, K. Wei, Experimental and numerical study of a passive thermal management system using flat heat pipes for lithium-ion batteries, App. Therm. Eng. 166 (2020) 114660, doi:10.1016/j.applthermaleng.2019.114660.

[17] J. Zhao, P. Lv, Z. Rao, Experimental study on the thermal management performance of phase change material coupled with heat pipe for cylindrical power battery pack, Exp. Therm. Fluid Sci. 82 (2017) 182–188, doi:10.1016/j.expthermflusci.2016.11.017.

[18] R. Zhao, J. Gu, J. Liu, An experimental study of heat pipe thermal management system with wet cooling method for lithium-ion batteries, J. Power Sources 273 (2015) 1089–1097, doi:10.1016/j.jpowsour.2014.10.007.

[19] Y. Lyu, A.R.M. Siddique, S.H. Majid, M. Biglarbegian, S.A. Gadsden, S. Mahmud, Electric vehicle battery thermal management system with thermoelectric cooling, Energy Reports 5 (2019) 822–827, doi:10.1016/j.egyr.2019.06.016.

[20] X. Li, Z. Zhong, J. Luo, Z. Wang, W. Yuan, G. Zhang, C. Yang, Experimental investigation on a thermoelectric cooler for thermal management of a Lithium-ion battery module, Int. J. Photoenergy. (2019) 3725364, doi:10.1155/2019/3725364.

[21] B. Mondal, C.F. Lopez, P.P. Mukherjee, Exploring the efficiency of nanofluids for lithium-ion battery thermal management, Int. J. Heat Mass Trans. 112 (2017) 779–794, doi:10.1016/j.ijheatmasstransfer.2017.04.130.

[22] Y. Hung, J. Chen, T. Teng, Feasibility Assessment of thermal management system for green power sources using nanofluid, J. Nanomaterials (2013) 321261 http://dx.doi.org/10.1155/2013/321261.

[23] T. Ohgaki, M. Matsuda, M. Matsumoto, Integrated Cooling System for Under-Floor High Voltage Devices in PHEV, SAE International, 2018, doi:10.4271/2018-01-1184.

[24] Tesla Motor Inc. Patent No: US20140178722A1 and Patent No: US20110212356A1 2021.

[25] D. Bohne, S. Fischer, E. Obermeier, Thermal conductivity, density, viscosity, and Prandtl-numbers of ethylene glycol-water mixtures, Phys. Chem. Chem. Phys. 88 (1984) 739–742.

[26] A. Bejan, S. Lorente, Design with Constructal Theory, John Wiley & Sons, Hoboken, 2008.

[27] A. Bejan, Freedom and Evolution: Hierarchy in Nature, Society, and Science, Springer, 2019.

[28] A. Bejan, S. Lorente, The constructal law and the evolution of design in nature, Phys. Life Rev. 8 (3) (2011) 209–240, doi:10.1016/j.plrev.2011.05.010.

[29] A. Bejan, S. Lorente, Current trends in constructal law and evolutionary design, Heat Transf. Asian Res. 48 (2019) 3574–3589, doi:10.1002/htj.21556.

[30] A. Bejan, S. Lorente, Constructal law of design and evolution: physics, biology, technology, and society, J. Appl. Phys 113 (15) (2013) 151301, doi:10.1063/1.4798429.
[31] S. Lorente, M. Hautefeuille, A. Sanchez–Cedillo, The liver, a functionalized vascular structure, Scientific Reports Nature Research 10 (2020) 16194, doi:10.1038/s41598-020-73208-8.
[32] R.S. Brum, J.V.A. Ramalha, M.K. Rodrigues, L.A.O Rocha, L.A. Isoldi, E.D. Dos Santos, Design evaluation of earth-air heat exchangers with multiple ducts, Ren. Energy. 135 (2019) 1371–1385, doi:10.1016/j.renene.2018.09.063.
[33] M.K. Rodrigues, R.S. Brum, J. Vaz, L.A.O. Rocha, E.D. Dos Santos, L.A. Isoldi, Numerical investigation about the improvement of the thermal potential of an Earth-Air Heat Exchanger (EAHE) employing the Constructal Design method, Ren. Energy. 80 (2015) 538–551, doi:10.1016/j.renene.2015.02.041.
[34] L.C. Victoria, V.F. Hermes, J. Vaz, J. Costi, W.C. Marques, L.A.O Rocha, E.D. Dos Santos, M.K. Rodrigues, C. Biserni, L.A. Isoldi, Methodology allying standard penetration test and era-interim data set for numerical simulations of earth-air heat exchangers, J. Adv. Res. Fluid Mech. Therm. Sci. 76 (2) (2020) 43–64, doi:10.37934/arfmts.76.2.4364.
[35] E. Estrada, M. Labat, S. Lorente, L.A.O Rocha, The impact of latent heat exchanges on the design of earth air heat exchangers, App. Therm. Eng. 129 (2018) 306–317, doi:10.1016/j.applthermaleng.2017.10.007.
[36] R.S. Brum, M. Labat, S. Lorente, Improving the performances of earth air heat exchangers through Constructal design, Int. J. Energy Res. 43 (2019) 1–12, doi:10.1002/er.4835.
[37] S. Lorente, A. Bejan, J.L. Niu, Phase change heat storage in an enclosure with vertical pipe in the center, Int. J. Heat Mass Transf. 72 (2014) 329–335, doi:10.1016/j.ijheatmasstransfer.2014.01.021.
[38] S. Lorente, A. Bejan, J.L. Niu, Constructal design of latent thermal energy storage with vertical spiral heaters, Int. J. Heat Mass Transf. 8 (2015) 283–288, doi:10.1016/j.ijheatmasstransfer.2014.09.077.
[39] A. Malley-Ernewein, S. Lorente, Analysis of thermochemical energy storage in an elemental configuration, Sci. Rep. Nature Res. 9 (2019) 15875, doi:10.1038/s41598-019-52249-8.
[40] A. Malley-Ernewein, S. Lorente, The shape of the elemental system in a porous medium designed for thermochemical energy storage, Int. J. Heat Mass Transf. 158 (2020) 119975, doi:10.1016/j.ijheatmasstransfer.2020.119975.
[41] S. Kim, S. Lorente, A. Bejan, Vascularized materials: tree-shaped flow architectures matched canopy to canopy, J. App. Phys. 100 (6) (2006) 305–354, doi:10.1063/1.2349479.
[42] M. Mosa, M. Labat, S. Lorente, Role of flow architectures on the design of radiant cooling panels, a constructal approach, Appl. Therm. Eng. 150 (2019) 1345–1352, doi:10.1016/j.applthermaleng.2018.12.107.
[43] M. Mosa, M. Labat, S. Lorente, Constructal design of flow channels for radiant cooling panels, Int. J. Therm. Sci. 145 (2019) 106052, doi:10.1016/j.ijthermalsci.2019.106052.
[44] S. Gungor, E. Cetkin, Enhanced temperature uniformity with minimized pressure drop in electric vehicle battery packs at high C-rates, Int. J. Therm. Sci. (2021) under review.
[45] E. Cetkin, S. Lorente, A. Bejan, Natural constructal emergence of vascular design with turbulent flow, J. Appl. Phys. 107 (2010) 114901, doi:10.1063/1.3430941.
[46] S. Lorente, A. Bejan, Svelteness, freedom to morph, and constructal multi-scale flow structures, Int. J. Therm. Sci. 44 (2005) 1123–1130, doi:10.1016/j.ijthermalsci.2005.08.011.
[47] A. Bejan, Convection Heat Transfer, 3rd edition, John Wiley & Sons, Hoboken, 2004.
[48] ANSYS Fluent Battery Module Manual, Release 15.0 2021.
[49] G.H. Kim, K. Smith, K.J Lee, S. Santhanagopalan, A. Peseran, Multi-domain modeling of Lithium-ion batteries encompassing multi-physics in varied length scales, J. Electrochem. Soc. 158 (8) (2011) A955–A969, doi:10.1149/1.3597614.
[50] M. Chen, G.A. Rincon-Mora, Accurate electrical battery model capable of predicting, IEEE Trans. Energy Conversion 21 (2) (2006) 504–511, doi:10.1109/TEC.2006.874229.
[51] O. Kalaf, D. Solyali, M. Asmael, Q. Zeeshan, B. Safaei, A. Askir, Experimental and simulation study of liquid coolant battery thermal management system for electric vehicles: a review, Int. J. Energy Res. 45 (5) (2020) 1–23, doi:10.1002/er.6268.